Materials Advances

ROYAL SOCIETY OF CHEMISTRY

PAPER

View Article Online
View Journal | View Issue

Cite this: *Mater. Adv.*, 2025, **6**, 8464

Tb^{3+} and Ce^{3+} as a functional couple for enhanced luminescence in YAG ceramics for X-ray imaging and high-power white LEDs and laser diodes

Anton Markovskyi,*[a] Warut Chewpraditkul,[b] Przemysław Gołębiewski,[a] Paweł Socha,[a] Helena Węglarz,[a] Agnieszka Szysiak,[a] Vitezslav Jary,[c] R. Kučerková,[c] Robert Tomala,[de] Akira Yoshikawa,[f] Shunshuke Kurosawa,[f] Ryszard Buczyński,[a] Weerapong Chewpraditkul[b] and Karol Bartosiewicz *[c]

The exposure of luminescent materials to X-ray radiation and high-power laser excitation results in significant heating, leading to thermal quenching and a corresponding reduction in phosphor efficiency. This study aimed to address this limitation by enhancing material efficiency while maintaining high thermal stability. YAG:Ce,Tb transparent ceramics were successfully fabricated *via* vacuum reactive sintering method, with moderate concentrations of Tb^{3+} ions (1, 5 and 10 at%) codopants. These ceramics exhibited a dense microstructure without micropores, achieving high transparency of 77–80% at 900 nm. The incorporation of Tb^{3+} ions, is evidenced by the systematic increase in lattice constants from 12.608 Å (YAG:Ce) to 12.615 Å (YAG:Ce,Tb10%) in accordance with Vegard's law. The phonon-assisted $Ce^{3+} \leftrightarrow Tb^{3+}$ bidirectional resonance mechanism, which facilitated energy transfer between Ce^{3+} and Tb^{3+} ions, was observed. The optimal transfer rate was observed at approximately 480 K. Beyond this temperature, the rate progressively accelerated, leading to accelerated decay times. Notably, YAG:Ce,Tb10% ceramics demonstrated a two-fold increase in radioluminescence intensity compared to uncodoped YAG:Ce ceramics. This substantial improvement in luminescence performance highlights the potential of YAG:Ce,Tb ceramics as highly efficient phosphors for X-ray imaging applications, offering enhanced brightness and energy transfer efficiency under high-temperature operating conditions. The Tb^{3+} codoping also enhanced Ce^{3+} emission, allowing for tuning of the correlated color temperature to a maximum of 6013 K, while maintaining a stable color rendering index of 69–73 and luminous efficacy of ~123 lm W^{-1}. It was shown that the luminous efficacy was not a constant parameter, but depended on the excitation laser power, initially increasing with power up to 0.5 W and then saturating. These results establish YAG:Ce,Tb transparent ceramics as highly promising materials for white LEDs due to their good thermal stability, tunable optical properties, and enhanced luminescence performance.

Received 9th May 2025,
Accepted 6th October 2025

DOI: 10.1039/d5ma00464k

rsc.li/materials-advances

1. Introduction

Inorganic scintillators effectively convert high-energy radiation into ultraviolet-visible or visible light. The scintillators are integral to numerous applications, such as their use in electromagnetic calorimeters for high-energy physics, non-destructive industrial inspections, X-ray imaging systems, and time-of-flight positron emission tomography (TOF-PET) in medical diagnostics.[1–4] Advancing the application of these scintillators requires the development of materials with enhanced efficiency, reduced afterglow and low production costs. Increased efficiency allows for a greater photon yield per radiation dose, producing higher-quality images without necessitating additional exposure.

[a] *Łukasiewicz Research Network - Institute of Microelectronics and Photonics, Aleja Lotników 32/46, 02-668, Warsaw, Poland. E-mail: anton.markovskyi@imif.lukasiewicz.gov.pl*
[b] *Department of Physics, Faculty of Science, King Mongkut's University of Technology Thonburi 126 Pracha-uthit, Thung-khru, Bangkok 10140, Thailand*
[c] *Institute of Physics of the Czech Academy of Sciences, Cukrovarnicka 10, 16200, Prague, Czech Republic. E-mail: bartosiewicz@fzu.cz*
[d] *Institute of Low Temperature and Structural Research Polish Academy of Sciences, Okólna 2, 50-422 Wrocław, Poland*
[e] *Faculty of Chemistry and Geosciences, Vilnius University, Naugarduko g. 24, 03225 Vilnius, Lithuania*
[f] *Institute for Materials Research, Tohoku University, 2-1-1 Katahira, Sendai 9808577, Japan*

Similarly, a reduced afterglow minimizes the temporal overlap of high-energy events and improves the signal-to-noise ratio, thereby enabling a quicker imaging process. These performance improvements are essential for optimizing both medical imaging and high-energy physics instrumentation.[5] High-resolution X-ray imaging demands a balance among spatial resolution, fine detail detection, sensitivity, and a strong signal-to-noise ratio.[6] The thickness of the scintillating material largely determines this balance, while thicker scintillators improve sensitivity by increasing X-ray attenuation and light yield, they may reduce spatial resolution due to light propagation and scattering. The scattering or diffusion of emitted light is a primary contributor to blurred X-ray images.[7,8] As a result, single crystal scintillators with low light scattering coefficients have become promising candidates for high-resolution applications. Their good light propagation characteristics reduce internal re-absorption and scattering, resulting in sharper, more detailed images.

The single crystals of Ce^{3+} doped $Y_3Al_5O_{12}$ (YAG) exhibit excellent spatial resolution, approximately 34.7 line pairs per millimeter (lp per mm).[9] The YAG crystalline structure exhibits excellent mechanical strength, allowing scintillation screens to be fabricated with thicknesses as low as 100 μm. This characteristic is especially advantageous in medical imaging and optoelectronic devices, where space and weight are critical factors.[10] Although single crystals offer advantages, polycrystalline ceramics are often chosen as an alternative.[11] Because of their faster and significantly cheaper production, easier fabrication of complex shapes, and more uniform dopant distribution.[11,12] The energy transfer efficiency from the host matrix to Ce^{3+} ions can be significantly improved by incorporating Gd^{3+} and Tb^{3+} ions as sensitizers. Tb^{3+} is considered an effective co-activator for facilitating energy transfer due to its absorption levels, which lie between the absorption of the host lattice and the emission of Ce^{3+}. Additionally, the $^5D_4 \rightarrow {}^7F_6$ transition of Tb^{3+} overlaps with the 4f $\rightarrow$ $5d_1$ absorption transition of the Ce^{3+} ion.[13–15]

The Tb^{3+} codoping in YAG:Ce is also relevant in the field of high-power lighting. YAG:Ce phosphor converters (pc) have demonstrated significant potential in various lighting applications, particularly in high-power lighting sources that require high thermal stability.[16–18] Phosphor in glass (PiG), single-crystal phosphors and ceramic phosphors are currently the most common phosphor conversion materials. Their thermal conductivity typically ranges between 0.1 and 30 W m^{-1} K^{-1}. Phosphor ceramics are preferable among them in terms of their overall photothermal characteristics.[19] The limitations of using such white LEDs/LDs for indoor lighting include a low color rendering index (CRI $<$ 80) and a high correlated color temperature (CCT $>$ 4000 K), which result from a lack of red components in the emission spectrum of YAG:Ce^{3+}. For instance, it has been widely observed that the emission wavelength of Ce^{3+} shifts to a longer wavelength, improving both the color CRI and CCT, when larger rare earth ions like Gd^{3+} and Tb^{3+} are used to substitute the dodecahedral site in YAG lattice.[20,21] In high-power LDs, maintaining the thermal stability of phosphor materials during operation remains a serious challenge. This instability arises from material heating under high energy excitation, which induces a thermal quenching process. To mitigate this, extensive research focuses on enhancing the phosphor's thermal stability by engineering its electronic structure. One effective strategy involves increasing the energy barrier between the conduction band minimum (CBM) and the lowest-energy 5d excited state ($5d_1$) of Ce^{3+} ions. In YAG:Ce, the partial substitution of Y^{3+} ions by larger Tb^{3+} ions enhances the crystal field strength, which increases the splitting of the 5d states of Ce^{3+}. This enlarge splitting elevates the energy barrier between the CBM and the Ce^{3+} $5d_1$ excited state, thereby reducing the probability of the thermal ionization process and improving the phosphor thermal stability under high-power energy excitation. However, the pronounced splitting of the Ce^{3+} $5d_1$ excited state substantially diminishes the Stokes shift. This in turn facilitates a reabsorption process leading to the quenching of the emission. The compositional engineering strategy is well-established and widely understood. However, there is a notable lack of systematic research on Tb^{3+}-codoped YAG:Ce systems with low Tb^{3+} ions concentrations ($\leq$10%). One of the key advantages of incorporating both Tb^{3+} and Ce^{3+} in a garnet host is the enhancement of luminescence intensity. This improvement arises from a synergistic energy transfer mechanism, which has the potential to significantly improve luminous efficacy (LE) in high-power LED applications.[22] Nevertheless, at high Tb^{3+} concentrations, the substantial overlap between the excitation and emission bands of Ce^{3+} ions leads to luminescence quenching, particularly at elevated temperatures. Consequently, a balanced substitution of Y^{3+} by Tb^{3+} by is essential for optimizing the performance of garnet phosphors. Addressing this knowledge gap and aiming to optimize the Ce^{3+}/Tb^{3+} concentration ratio in YAG transparent ceramics, a series of transparent ceramics were prepared, including undoped and Ce^{3+} (0.5 at%) doped YAG as reference samples as well as Tb^{3+}-codoped YAG:Ce 0.5 at%, with Tb^{3+} concentrations 1, 5 and 10 at%. A systematic study was conducted on the influence of the Ce^{3+}/Tb^{3+} concentration ratio on microstructure, phase purity, absorption, transmittance, luminescence, and scintillation characteristics, along with the underlying bidirectional energy transfer mechanism between Ce^{3+} and Tb^{3+} ions. Moreover, the photoconversion parameters of transparent ceramics were evaluated. Additionally, the thermal stability of Ce^{3+} emission and the efficiency of the bidirectional $Tb^{3+} \leftrightarrow Ce^{3+}$ energy transfer process were analyzed over a temperature range from 77 to 767 K.

2. Experiment

2.1. Sample preparation

A set of YAG:Ce 0.5 at%,Tb (0, 1, 5, 10 at%) transparent ceramics was prepared. Initially, aqueous slurries of Y_2O_3 (4N), Al_2O_3 (4N), CeO_2 (4N) and Tb_4O_7 (4N) were prepared by blending the powders in a planetary mill with DolapixCE 64 dispersing agent, DuramaxB-1000 binder, and a laboratory-made octakis-(tetramethylammonium)-T8-silsesquioxane hydrate (Octaanion)

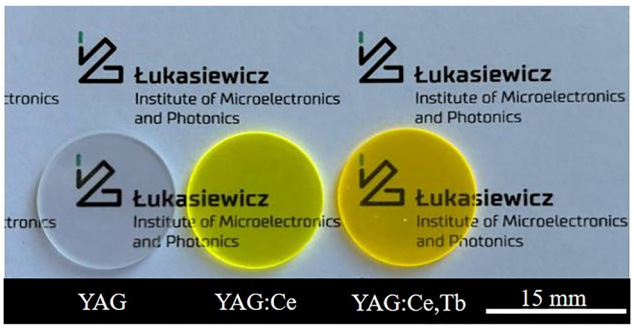

Fig. 1 Photograph of mirror-polished YAG, YAG:Ce, and YAG:Ce,Tb transparent ceramics with 1 mm thickness under daylight.

sintering aid. These homogeneous slurries were then sprayed into liquid nitrogen to form granulates, which were subsequently lyophilized for approximately 10–12 hours. The obtained granulates were pressed uniaxially in molds into disk shapes measuring 20 mm in diameter and approximately 4 mm in thickness. The samples underwent calcination in air at 1220 K to remove organic additives, followed by vacuum sintering at 1988 K for 6 hours. Subsequently, the samples were annealed in air at 1870 K for 2 hours to minimize oxygen-vacancy concentration. Finally, ceramics were cut and polished to dimensions of $4 \times 4 \times 1$ mm^3. Fig. 1 is the photograph of the as-sintered YAG, YAG:Ce, and YAG:Ce,Tb ceramics.

2.2. Methods

X-ray diffraction (XRD) was utilized for qualitative phase analysis of the ceramics. The measurements were conducted using a Rigaku SmartLab 3-kW X-ray diffractometer, equipped with a copper X-ray tube operating at 40 kV and 30 mA, along with a D/tex Ultra 250 solid-state detector. Phase analysis was conducted on bulk samples in continuous mode, employing Bragg–Brentano geometry ($\theta/2\theta$ scan) across an angular range of 5°–120° (2θ) with a scan step of 0.01° and a speed of 1.2° min^{-1}. XRD data analysis was performed using Rigaku PDXL 2 software. To perform a microscopic examination, mirror-polished samples were thermally etched in air at 1870 K for 30 minutes to expose the grain boundaries. The ceramic microstructures were then analyzed using a scanning electron microscope (SEM) (Carl Zeiss CrossBeam Workstation AURIGA, Oberkochen, Germany). Transmittance spectra were recorded with a Jasco V-730 UV-vis spectrometer in the 200–2000 nm spectral range at 300 K.

Photoluminescence excitation (PLE) and photoluminescence emission (PL) spectra were measured by a custom-made spectrofluorometer 5000 M (Horiba Jobin Yvon, Wildwood, MA, USA) using a steady-state laser-driven xenon lamp (Energetic, a Hamamatsu Company) as the excitation source. The detection part of the setup involved a single-grating monochromator and a photon-counting detector TBX-04 (Hamamatsu). The PL and PLE spectra were corrected for the experimental distortion.

PL decay curves were measured by a custom-made spectrofluorometer 5000 M (Horiba Jobin Yvon, Wildwood, MA, USA) under excitation with ns-pulsed nanoLED light source and operated in time-correlated single-photon counting mode (Horiba Scientific). The detection part of the setup involved a single-grating monochromator and a photon-counting detector TBX-04 (Hamamatsu). The convolution procedure was applied to the PL decay curves to determine true decay times (SpectraSolve software package, Ames Photonics). Variable temperatures were accomplished by liquid nitrogen bath cryostats (LakeShore Cryotronics, environment by Janis).

Light yield (LY) measurements were performed using a photomultiplier tube (PMT) under excitation with 662 keV γ-rays (^{137}Cs source). Each ceramic sample was coupled to a Hamamatsu R6231 PMT window with silicone grease and covered with several layers of Teflon tape to increase light collection. The pulse height spectra of γ rays were recorded with a PC-based multichannel analyzer (MCA) Tukan8k after pulse processing by a preamplifier and a spectroscopy amplifier set at 2 μs shaping time constant. Scintillation decays were measured under excitation with 662 keV γ rays by coupling each ceramic sample to a Hamamatsu R7600U-200 PMT and recording the scintillation time profiles with a TDS3054B digital oscilloscope.

Radioluminescence (RL) spectra were measured by a custom-made spectrofluorometer 5000M (Horiba Jobin Yvon, Wildwood, MA, USA) using the Mo X-ray tube (40 kV, 15 mA, Seifert) as the excitation source. The setup's detection part involved a single-grating monochromator and a photon-counting detector TBX-04 (Hamamatsu). Measured RL spectra were corrected for the spectral dependence of detection sensitivity.

In the photoconversion experiments, ceramic samples with dimensions of $4 \times 4 \times 1$ mm^3 were placed on a collimator lens to ensure that the beam spot from the diode or laser illuminated the maximum area of the square sample. Measurements were performed in transmission mode. The 455nm LED (FWHM = 21.6 nm) was used for excitation. The blue excitation optical power was maintained at 0.6 W. For the power-dependent experiment, a 445 nm laser diode (LD) from CNI Lasers was used as the excitation source.

Measurements were conducted using a Gigahertz BTS-256LED spectrometer equipped with an integrating sphere for chromaticity parameters. The CIE 1931 coordinates (x, y), CRI and CCT were computed using the S-BTS256 software. All experiments were carried out at room temperature (RT).

3. Results and discussion

3.1. Structural analysis and optical transmittance of YAG:Ce, Tb ceramics

The XRD patterns of YAG:Ce,Tbx% (x = 0, 1, 5 and 10) transparent ceramics are shown in Fig. 2a. The crystal structure remains unchanged, validated through comparison with reference data: PDF No. 82-575. Analysis of the Rietveld refinement of XRD patterns indicates that all samples have been sintered in the pure cubic space group $Ia\bar{3}d$ (No. 230), with no presence of secondary phases (Table 1).

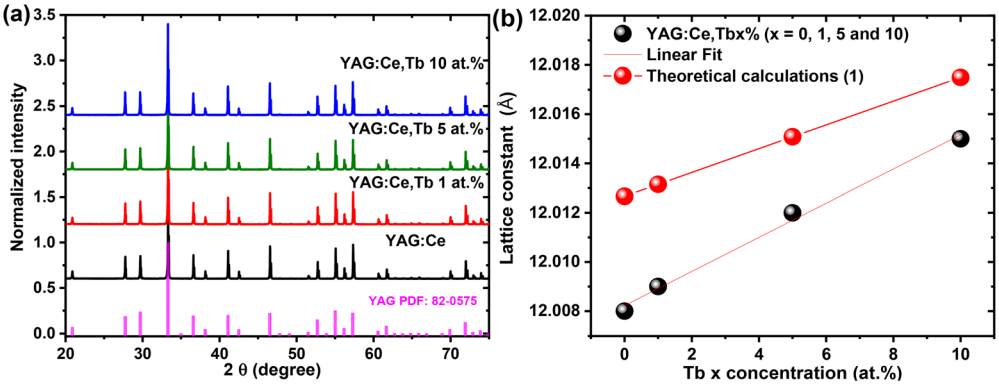

Fig. 2 (a) XRD patterns of YAG:Ce,Tb*x*% (*x* = 0, 1, 5 and 10) transparent ceramics; (b) dependence of lattice constant on Tb concentration in YAG:Ce,Tb*x*% (*x* = 0, 1, 5 and 10) ceramics.

As the concentration of Tb^{3+} dopant increases in YAG:Ce, Tb*x*% (*x* = 0, 1, 5 and 10) ceramics, the lattice constant increases due to the well-known effect of displacement of smaller Y^{3+} ions (ionic radius of Y_{VIII} = 1.019 Å) by larger Tb^{3+} ions (ionic radius of Tb_{VIII} = 1.04 Å) into the dodecahedral site in the garnet lattice.[23] Fig. 2b illustrates the experimental dependence of the lattice constant a_0 on the increasing concentration of larger Tb^{3+} ions, in comparison with theoretical predictions. The unit cell parameters of garnets can be determined using analytical expressions derived from lattice geometry. These expressions account for the effective ionic radii of the constituent ions[24]

The lattice parameter of garnet structures can be described by the following analytical expression (eqn (1)):

$$a = b_1 + b_2 \cdot r_c + b_3 \cdot r_a + b_5 \cdot r_c \cdot r_a + b_6 \cdot r_c \cdot r_d + b_4 \cdot r_d \qquad (1)$$

where the coefficients are given as: b_1 = 7.02954, b_2 = 3.31277, b_3 = 2.49398, b_4 = 3.34124, b_5 = −0.087758b, and b_6 = −1.38777. The variables r_c, r_a, and r_d represent the effective ionic radii of cations occupying the respective sites in the garnet lattice (r_c (Tb^{3+})) = 1.04 Å, r_a (Al^{3+}) = 0.55 Å, and r_d (Al^{3+}) = 0.39 Å.[25,26] The calculated values are summarized in Table 1. Fig. 3 shows SEM micrographs of thermally etched surfaces of YAG:Ce,Tb*x*% (*x* = 0, 1, 5 and 10) ceramics. The ceramics synthesized at 1988 K exhibit a homogeneous microstructure, characterized by uniform and well-defined grain boundaries. Notably, no evidence of secondary phases or amorphous (glassy) regions is observed, indicating high phase purity and effective densification of the material. EDS analysis confirms a homogeneous elemental distribution both within the grains and at the grain boundaries. The grain size distribution and average grain size of the constituent phases in YAG:Ce,Tb*x*% (*x* = 0, 1, 5 and 10) ceramics were evaluated using the linear intercept method applied to SEM images of the thermally etched surface. Substituting larger rare-earth ions (such as Nd^{3+}, Tb^{3+}, Yb^{3+}, or Gd^{3+}) for Y^{3+} in the YAG lattice introduces lattice strain due to the size mismatch. This strain promotes the segregation of dopant ions to grain boundaries during sintering. Their presence at the boundaries impedes grain boundary motion through the solute drag effect, a mechanism where migrating boundaries must overcome the energy associated with solute-boundary interactions. As a result, grain growth is suppressed, leading to finer and more uniform grains, especially at higher dopant concentrations. However, at the highest Tb^{3+} concentration in YAG ceramics, the grain growth mechanism transitions from solute drag to more complex processes, which results in an increase of the grain size.[27–29]

3.2. Transmittance properties

Fig. 4a presents the RT transmittance spectra of the synthesized ceramics. The Tb^{3+}-doped YAG:Ce ceramics exhibit high optical transparency, with transmittance values ranging from 77% to 80% at 900 nm. In the infrared region, each transmission spectrum exhibits three prominent peaks at approximately 1853 nm ($^7F_6 \rightarrow {}^7F_1$), 1953 nm ($^7F_6 \rightarrow {}^7F_2$), and 2179 nm ($^7F_6 \rightarrow {}^7F_3$). The intensity of these peaks increases with the rising concentration of Tb^{3+} ions.[30] Detailed assignment for the absorption lines is listed in Table 2. Fig. 4b displays the RT absorption spectra of YAG:Ce,Tb*x*% (*x* = 0, 1, 5 and 10) transparent ceramics in the 200–700 nm range. The characteristic absorption bands of Ce^{3+} ions in the YAG lattice are observed at 340 nm and 450 nm, corresponding to the 4f → $5d_2$ and 4f → $5d_1$ electronic transitions, respectively. The absorption observed in the

Table 1 Rietveld refinement of lattice parameters and volume of YAG:Ce,Tb*x*% (*x* = 0, 1, 5 and 10) transparent ceramics

Sample	Composition	*a* = *b* = *c* (Å)	*V* (Å^3)	*a* (Å) calculated
YAG:Ce	$Y_{2.985}Ce_{0.015}Al_5O_{12}$	12.008	1731.4(1)	12.0127
YAG:Ce,Tb1%	$Y_{2.955}$ $Ce_{0.015}Tb_{0.03}$ Al_5O_{12}	12.009	1731.7(1)	12.0131
YAG:Ce,Tb5%	$Y_{2.835}$ $Ce_{0.015}Tb_{0.15}$ Al_5O_{12}	12.012	1732.98(1)	12.0151
YAG:Ce,Tb10%	$Y_{2.685}$ $Ce_{0.015}Tb_{0.3}$ Al_5O_{12}	12.015	1734.6(1)	12.0175

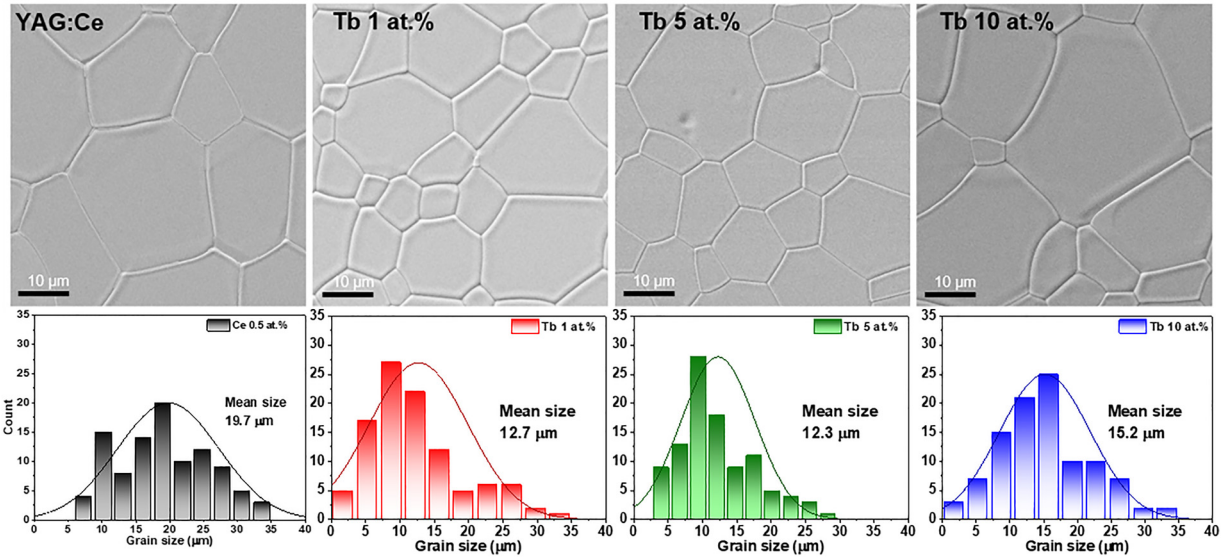

Fig. 3 SEM images and grain size distribution in YAG:Ce,Tb*x*% (*x* = 0, 1, 5 and 10) ceramics obtained by vacuum sintering at *T* = 1988 K.

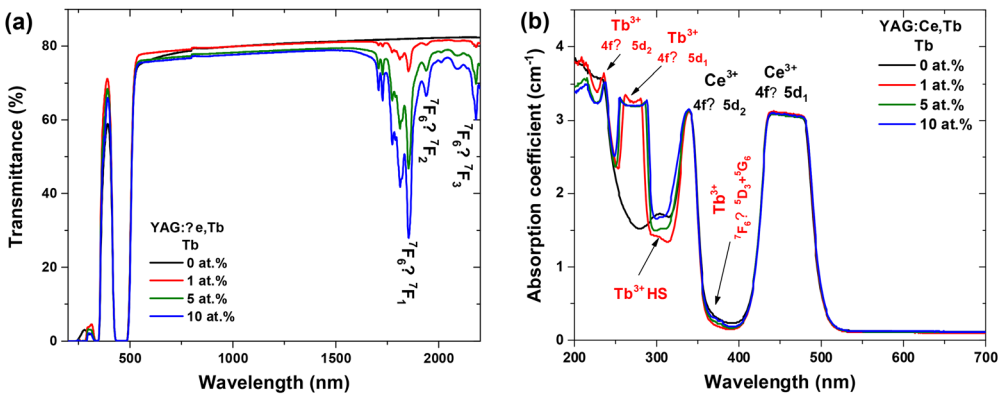

Fig. 4 (a) Optical transmittances and (b) absorption spectra of YAG:Ce,Tb*x*% (*x* = 0, 1, 5 and 10) transparent ceramics.

Table 2 Summary of the absorption transitions in the YAG:Ce,Tb*x*% (*x* = 0, 1, 5 and 10) ceramics

Ion	Absorption transition	Band position (nm)
Tb^{3+}	$4f \rightarrow 5d_2$	224
	$4f \rightarrow 5d_1$	270
	$^7F_6 \rightarrow {}^5D_3$	373
	$^7F_6 \rightarrow {}^5G_6$	372 378
	$^7F_6 \rightarrow {}^7F_1$	1853
	$^7F_6 \rightarrow {}^7F_2$	1939
	$^7F_6 \rightarrow {}^7F_3$	2179
Ce^{3+}	$4f \rightarrow 5d_2$	340
	$4f \rightarrow 5d_1$	450

ultraviolet region between 200 and 300 nm for YAG:Ce, can be primarily attributed to the charge-transfer transition from O^{2-} to Ce^{4+}.[31] This involves the transfer of electrons from the oxygen 2p to the cerium 4f energy levels. The presence of Ce^{4+} in YAG:Ce ceramics sintered under the same conditions was previously confirmed by EPR measurements, and the Ce^{4+}/Ce^{3+} ratio was estimated to be 2.6.[31] It is worth noting that the stabilization of Ce^{4+} ions within the YAG host lattice is promoted by the formation of oxygen vacancies, which serve as a mechanism to maintain charge neutrality and structural integrity.

The higher-energy $4f \rightarrow 5d_{3,4}$ transitions of Ce^{3+} ions as well as structural defects further increase the absorption intensity in the UV spectral range.[31] In addition, the absorption spectra contain sets of bands belonging to the transitions of Tb^{3+} ions. Namely, the bands centered around ~224 and ~270 nm belong to the low spin-allowed (LS) $4f \rightarrow 5d_2$ and $4f \rightarrow 5d_1$ absorption transitions of Tb^{3+} ions. The spin-forbidden (HS) $4f \rightarrow 5d_1$ transition within Tb^{3+} ions is centered at 325 nm. The lines centered at 373 nm are attributed to the $^7F_6 \rightarrow {}^5D_3 + {}^5G_6$ absorption transitions of Tb^{3+} cations.[14]

3.3. Photoluminescence properties

Fig. 5 displays the PLE and PL spectra of YAG:Ce,Tb*x*% (*x* = 0, 1, 5 and 10) ceramics. The PLE spectra recorded for Ce^{3+} emission at 530 nm (Fig. 5a) and Tb^{3+} emission at 544 nm (Fig. 5b)

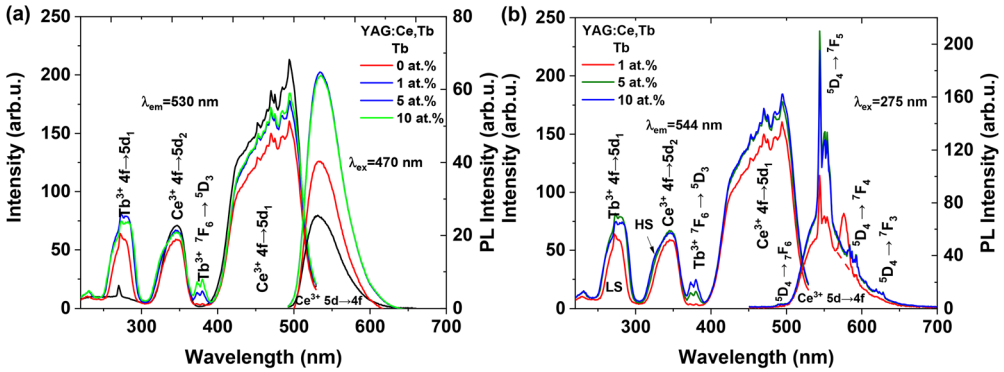

Fig. 5 (a) PLE spectra for Ce^{3+} emission at 530 nm and PL spectra excited into Ce^{3+} ions at 470 nm in YAG:Ce,Tb*x*% (*x* = 0, 1, 5 and 10) ceramics; (b) PLE spectra for Tb^{3+} emission at 544 nm and PL spectra excited into Tb^{3+} ions at 275 nm. The PL and PLE spectra of the singly doped Ce^{3+} and Tb^{3+} ceramics are presenten in Fig. S1 in the SI.

display distinct excitation bands attributable to both Ce^{3+} and Tb^{3+} ions, which are in agreement with the absorption spectra shown in Fig. 4b. The appearance of Tb^{3+} absorption bands within the Ce^{3+} excitation spectra and Ce^{3+} absorption bands within the Tb^{3+} excitation spectra provide evidence for the bidirectional energy transfer process between Tb^{3+} to Ce^{3+} ions. This observation underscores the role of Tb^{3+} ions in enhancing Ce^{3+} emission *via* a nonradiative transfer mechanism optimizing the luminescent efficiency of these materials.[14,32–36] The PL spectra of YAG:Ce,Tb*x*% (*x* = 0, 1, 5 and 10) excited into Ce^{3+} ions at 470 nm show a broad band peaking around 530 nm related to the $5d_1 \rightarrow 4f$ ($^2F_{5/2}$, $^2F_{7/2}$) emission transition in the Ce^{3+}. The absence of Tb^{3+} emission lines in the spectra suggests that the energy states of Ce^{3+} ($5d_1$) and Tb^{3+} ($^5D_4$) are in optimal resonance. This resonance facilitates an efficient, bidirectional energy exchange mechanism between Tb^{3+} and Ce^{3+} ions. The process is ultimately dominated by Ce^{3+} emission, attributed to the allowed $5d_1 \rightarrow 4f$ emission transition within Ce^{3+} ions.[19,20,36]

The PL spectra excited into Tb^{3+} ions at 275 nm show Tb^{3+} ions 4f → 4f emission lines at ~490, ~544, ~588 and ~624 nm corresponding to $^5D_4 \rightarrow {}^7F_{(6,5,4,3)}$ transitions and Ce^{3+} ions emission bands, which intensity increase with increasing of Tb^{3+} ions concentration. The relatively high Tb^{3+} ions concentration causes strong quenching emission from $^5D_3$ energy state due to $^5D_3$–$^5D_4$ cross relaxation interaction.[37] The PL spectra excited at 275 nm, corresponding to the Tb^{3+} 4f → $5d_1$ LS transition show characteristic Tb^{3+} emission lines associated with the $^5D_4 \rightarrow {}^7F_6$ (~480 nm), $^5D_4 \rightarrow {}^7F_5$ (~550 nm), $^5D_4 \rightarrow {}^7F_4$ (~590 nm), $^5D_4 \rightarrow {}^7F_3$ (~625 nm) and $^5D_4 \rightarrow {}^7F_2$ (~680 nm) transitions. Additionally, a broad emission band spanning from 500 to 700 nm is observed, originating from the $5d_1 \rightarrow 4f$ transition of Ce^{3+} ions.

The variation in emission profiles depending on the excitation wavelength (*i.e.*, Ce^{3+} at 470 nm and Tb^{3+} at 275 nm) provides an insight into the efficiency of the energy transfer process between Tb^{3+} and Ce^{3+} ions. This finding highlights that the energy transfer efficiency is significantly influenced by the concentration of Tb^{3+} ions. Specifically, the bidirectional energy transfer between Tb^{3+} and Ce^{3+} is restricted to ions that are in close spatial proximity. In such cases, the excitation energy from Tb^{3+} is efficiently transferred to Ce^{3+}, where the emission is ultimately observed. Conversely, for Tb^{3+} ions that are not spatially coupled and thus not in resonance with Ce^{3+} ions, the excitation energy remains localized within the Tb^{3+} ions and terminates with Tb^{3+} emission. As a result, the restricted spatial interaction ensures that excitation energy is either confined to Tb^{3+} ions (leading to Tb^{3+} emission) or partially transferred to Ce^{3+} ions that are in resonance, resulting in a combination of emissions from both Tb^{3+} and Ce^{3+} ions under excitation into Tb^{3+} excitation bands.[19,20]

Fig. 6a presents the PL decay curves of YAG:Ce, Tb*x*% (Tb = 0, 1, 5, 10) ceramics (λ_{ex} = 450nm, λ_{em} = 544nm) measured at RT. For the samples without Tb^{3+} ions and with low *x* = 1% concentration a single exponential decay is observed with a decay time of ~ 70 ns (eqn (2)). With an increase in Tb^{3+} ions concentration up to 5%, the initial part of the decay curve exhibits a non-exponential profile, thus, the double-exponential fit is used for the qualitative description of two components: τ_1 = 41 ns and τ_2 = 71 ns.

$$I(t) = \sum I_i \exp[-t/\tau_i] + B, i = 1 \text{ to } 2, \quad (2)$$

the parameters I_i and τ_i stand for the pre-exponential factor and decay time, respectively, in the *i*th decay component.

Due to the double-exponential fitting of the decay curves, effective decay time, $\tau_{effective}$, is introduced for consideration, defined by the equation (eqn (3)):

$$\tau_{effective} = \frac{\sum A_i \tau_i^2}{\sum A_i \tau_i} \quad (3)$$

where A_i is the amplitude and τ_i is the decay time value of the *i*-th component from the fit.

The non-exponential character of the decay curves provides further evidence of the bidirectional energy transfer process between Ce^{3+} and Tb^{3+} ions, as depicted in the simplified energy transfer scheme (Fig. 7). The energy transfer dynamics between Ce^{3+} and Tb^{3+} ions exhibit a complex interplay,

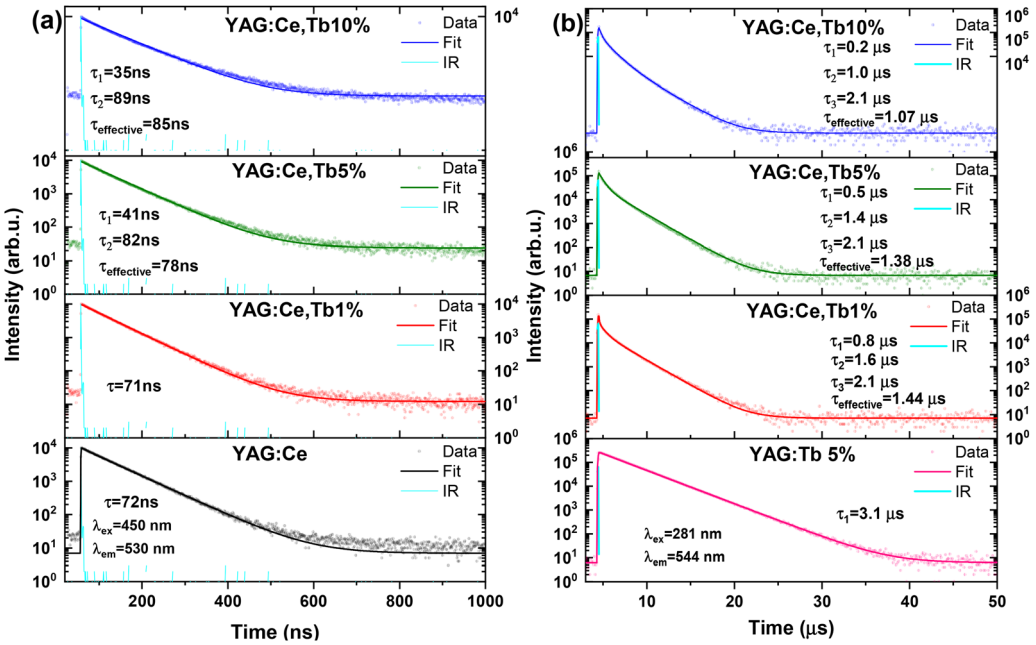

Fig. 6 (a) Prompt $5d_1 \rightarrow 4f$ decay curves of the Ce^{3+} luminescence measured at λ_{em} = 530 nm and λ_{ex} = 450 nm; (b) decay curves of Tb^{3+} ($^5D_4 \rightarrow {}^7F_5$) emission measured at λ_{em} = 544 nm and λ_{ex} = 281 nm for YAG:Ce,Tb*x*% (*x* = 0, 1, 5 and 10) ceramics samples.

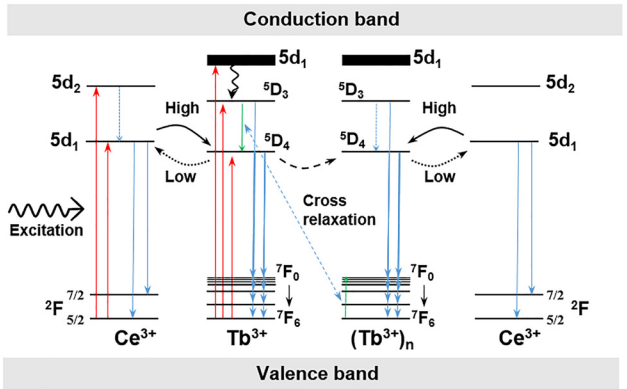

Fig. 7 Simplified energy diagram for Tb^{3+} and Ce^{3+} ions in $Y_3Al_5O_{12}$. The red arrows indicate the absorption of photons, leading to excitation to higher energy levels. The black wavy arrow illustrates the relaxation process, while the black curved dotted arrows depict energy transfer processes. The blue dash arrows represent the cross-relaxation between neighboring Tb^{3+} ions, and the blue arrows signify radiative de-excitation mechanisms (emission of photons).

wherein the initial excitation energy absorbed by Ce^{3+} undergoes a bidirectional transfer mechanism. Specifically, while energy is efficiently transferred from Ce^{3+} to Tb^{3+} ions through resonant energy transfer, a significant back-transfer process to Ce^{3+} occurs due to the energy level match between both ions. This energy transfer cycle influences the decay kinetics of Ce^{3+}, significantly accelerating the fast decay components while decelerating the slow components. Consequently, this dynamic interaction significantly suppresses the emission intensity of Tb^{3+} ions at higher concentrations. Such behavior underscores the intricate balance of energy transfer processes between Ce^{3+} and Tb^{3+}, highlighting the cooperative effects that govern their luminescent properties in Tb^{3+} ion concentrated systems. For further analysis of the $Tb^{3+} \rightarrow Ce^{3+}$ energy transfer process, the PL decay measurements were performed for Tb^{3+} ($^5D_4 \rightarrow {}^7F_5$) emission measured at λ_{em} = 544 nm under excitation into $4f \rightarrow 5d_1$ transition of Tb^{3+} at 281 nm (Fig. 6b). The decay time of Tb^{3+} ions in YAG:Tb5% demonstrate single-exponential decay kinetics with decay time around 3 μs typical for Tb^{3+} ions in YAG host.[38] The PL decay characteristics of Tb^{3+} ions emission at 544 nm in Tb^{3+},Ce^{3+} co-doped ceramics exhibit significant acceleration, demonstrating a multi-exponential behavior. Analysis of YAG:Ce0.5%, Tb*x*% (*x* = 0, 1, 5, 10) ceramics reveals that the decay time systematically decreases with increasing Tb^{3+} ion concentration, providing evidence for concentration-dependent energy transfer mechanisms between Tb^{3+} and Ce^{3+} ions. The higher Tb^{3+} ions concentration enhances the probability of resonant energy transfer as the spatial proximity between Tb^{3+} and Ce^{3+} ions decreases at higher Tb^{3+} concentrations. The observed correlation between dopant concentration and energy transfer efficiency suggests a direct relationship between the local ion density and the quantum mechanical coupling strength facilitating the transfer process. Quantitative analysis of the decay time characteristics is comprehensively presented in Table 3.

Oxygen vacancies play a key role in stabilizing Ce^{4+} ions as previously discussed in Section 3.2. The trapped electron in an F^+ center creates localized electronic states within the bandgap of the YAG structure.[39] Fig. 8a shows the normalized emission spectra of the F^+ center with a maximum at around 380 nm to demonstrate the low intensity of its emission, compared to the Tb-codoped sample, where F^+ emission is strongly overlapped

Table 3 PL decay time values for Ce^{3+} and Tb^{3+} emissions

	Ce^{3+} ions decay (λ_{ex} = 450nm, λ_{em} = 530nm)		Tb^{3+} ions decay (λ_{ex} = 281nm, λ_{em} = 544nm)		
Sample	τ_1 ns (I%)	τ_2 ns (I%)	τ_1 μs	τ_2 μs	τ_3 μs
YAG:Ce	72 (100)	n/a	n/a	n/a	n/a
YAG:Tb 5%	n/a	n/a	3.1	n/a	n/a
YAG:Ce,Tb1%	71 (100)	n/a	0.8	1.6	2.1
YAG:Ce,Tb5%	41 (17)	82 (83)	0.5	1.4	2.1
YAG:Ce,Tb10%	35 (16)	89 (86)	0.2	1	2.1

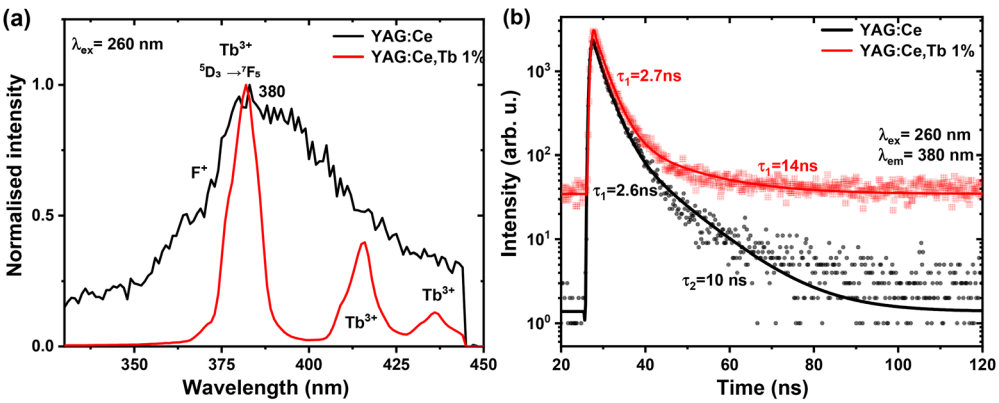

Fig. 8 (a) RT photoluminescence spectra of F^+ center excited at 260 nm, and (b) photoluminescence decay kinetics of F^+ center at 380 nm excited at 260 nm.

by a dominant peak centered at 382 nm, attributed to the $^5D_3 \rightarrow {}^7F_5$ transition of Tb^{3+} ions.[40,41]

Fig. 8b demonstrates the decay curves of the F^+ emission (λ_{ex} = 260 nm, λ_{em} = 380 nm) measured at RT and fitted using a double-exponential function as described in eqn (2). The primary decay component, corresponding to the allowed 1B → 1A singlet–singlet transition of F^+ centers, has a decay time of approximately 2 ns in the YAG:Ce host.[42] The presence of a slower component (τ_2 = 10 ns) in the YAG:Ce sample indicates disturbances or the aggregation of F^+ centers as well as the energy transfer process to the surrounding Ce^{3+} ions, which can absorb (4f → $5d_2$ transition) the F^+-center-related emission near the short-wavelength side. The slower component in the Tb^{3+}-codoped sample decelerated up to 14 ns, which can show complex interactions between oxygen vacancy and $^5D_3$ energy state of Tb^{3+} ions.

3.4. Temperature-dependent characteristics

Fig. 9a–d provides a detailed analysis of the temperature-dependent Ce^{3+} emission spectra recorded under 450 nm excitation corresponding to the 4f → $5d_1$ absorption band. The spectra were measured over a temperature range (77–767 K) for YAG:Ce,Tb*x*% (*x* = 0, 1, 5 and 10) ceramics. In YAG:Ce ceramics, a significant increase in emission intensity is observed over the temperature range of 77–400 K. However, in Tb^{3+}-codoped samples, this enhancement occurs only between 77 and 300 K and remains negligible, see Fig. 10. To eliminate potential interference from thermoluminescence (TL) effects and ensure that the observed intensity variations result solely from intrinsic temperature-dependent phenomena, the PL spectra were measured in a high-to-low temperature sequence (767 K to 77 K). This approach ensures the reliability of the thermal behavior analysis of Ce^{3+} emission in YAG:Ce,Tb ceramics.[43]

The mechanism underlying the progressive increase in the emission intensity with increasing temperature can be attributed to phonon-assisted nonradiative energy transfer (PA-NET). This process occurs between two distinct Ce^{3+} centers, *i.e.* the donor sites, comprising distorted Ce^{3+} centers (characterized by interactions with antisite defects, interstitial non-stoichiometric yttrium, lattice vacancies, and structural distortions at grain boundaries, resulting in lowered $5d_1$ state energy), and the acceptor sites, consisting of regular Ce^{3+} centers (occupying dodecahedral c-sites with D_2 symmetry in the crystal lattice).[31,44] This phenomenon is particularly pronounced in transparent ceramics, where the material exhibits challenges associated with Ce^{3+} ion segregation and agglomeration at grain boundary interfaces. The inhomogeneous distribution of Ce^{3+} ions, primarily manifested through segregation processes during sintering, significantly impacts the optical and luminescent properties as it can lead to localized variations in activator concentration.[31] Therefore, in transparent ceramics, the degree of disorder among Ce^{3+} ions is significant, resulting in inhomogeneously broadened emission and excitation bands. This indicates that Ce^{3+} ions are not uniformly excited within the transparent ceramic matrix, which in turn leads to reduced emission intensity at lower temperatures. As temperature rises, the excitation and emission bands broaden (see Fig. 9a and b, lower panels),[45–47] allowing both regular and disordered Ce^{3+}

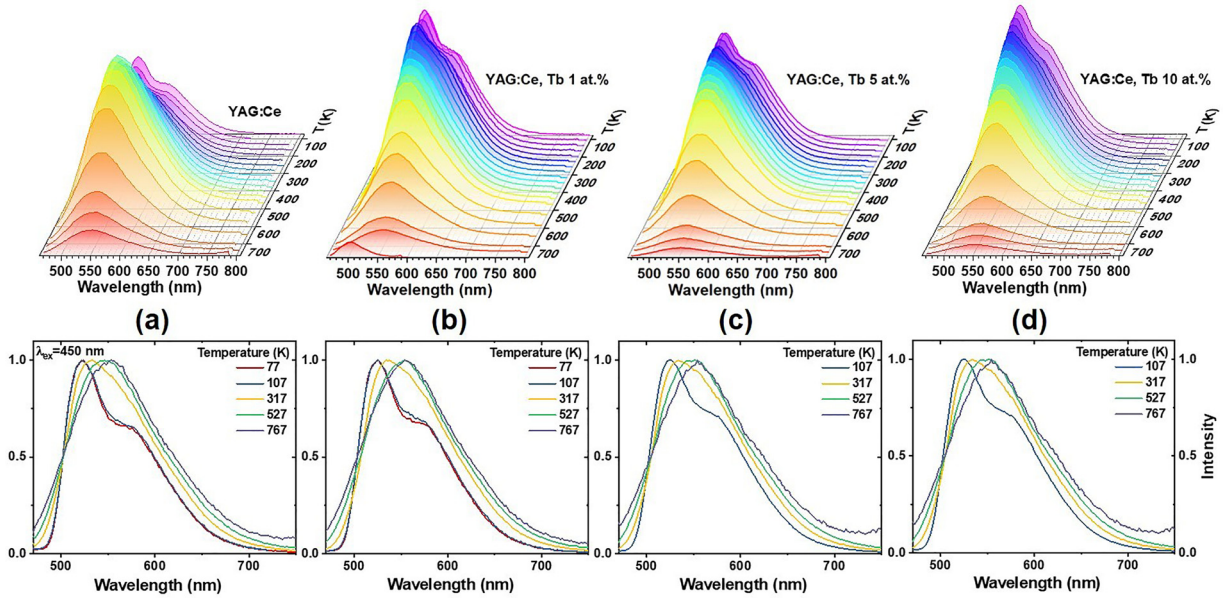

Fig. 9 PL spectra of Ce^{3+} ions in YAG:Ce,Tb*x*% (*x* = 0, 1, 5 and 10) ceramic samples (a–d) excited at 450 nm and recorded in the 77–767 K temperature range.

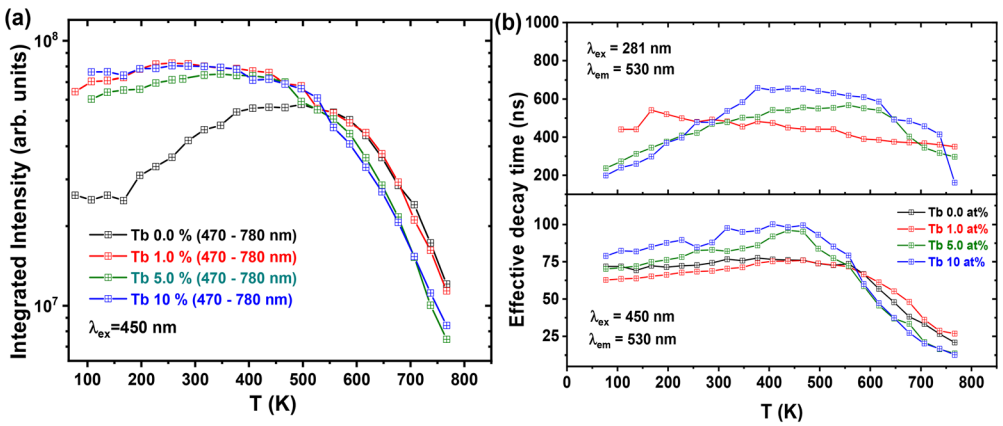

Fig. 10 (a) temperature dependence of the integrated Ce^{3+} emission intensity under excitation into 4f → $5d_1$ absorption transition at 450 nm in the temperature range 77–767 K; (b) temperature dependence of photoluminescence decay times for the Ce^{3+} emission at 530 nm under excitation into 4f → $5d_1$ absorption transition of Tb^{3+} at 281 nm (upper panel) and excitation into 4f → $5d_1$ absorption transition at 450 nm (lower panel).

ions to be more efficiently excited. Furthermore, the increased temperature enhances the energy of the host lattice phonons, facilitating the bridging of the energy mismatch between regular and disordered Ce^{3+} ions, thereby enabling the PA-NET process. A detailed explanation of this mechanism can be found in ref. 44. The occurrence of the PA-NET process is further supported by a minor increase in emission intensity with elevated temperatures and the presence of Tb^{3+} ions. The incorporation of Tb^{3+} ions significantly enhances crystal field strength which induces a downward shift in the energetic position of the $5d_1$ electronic state of Ce^{3+} ions in their regular lattice sites. This modification facilitates the energetic convergence between Ce^{3+} ions occupying both regular and disordered crystallographic positions. As a consequence, the excitation efficiency of Ce^{3+} ions exhibits enhanced performance at reduced temperatures, requiring lower-energy phonons to facilitate the PA-NET process. The enhanced emission intensity observed in Tb^{3+}-codoped YAG:Ce ceramics, relative to their undoped YAG:Ce counterpart, can be attributed to the bidirectional energy transfer processes between Ce^{3+} and Tb^{3+} ions (Fig. 10a). The excitation of Ce^{3+} ions initiates an energy transfer cascade wherein the excitation energy preferentially migrates to neighboring Tb^{3+} ions through resonant coupling mechanisms. This preferential pathway demonstrates higher efficiency compared to alternative routes involving Ce^{3+}–Ce^{3+} pair interactions at ceramic grain boundaries or energy dissipation through structural defect sites, where non-radiative decay processes dominate. The energy transfer dynamics are governed by a bidirectional, non-radiative interaction between

Tb^{3+} and Ce^{3+} ions, most plausibly mediated by dipole–dipole and higher-order multipolar coupling mechanisms. Upon excitation, energy can be transferred from the $^5D_4$ excited state of $Tb^{3+}$to the 5d levels of Ce^{3+}, resulting in enhanced Ce^{3+}emission intensity. Under specific excitation conditions and particularly at elevated Tb^{3+}concentrations, a reverse energy transfer process from excited Ce^{3+}back to Tb^{3+} is also observed. This bidirectional transfer behavior leads to a dynamic redistribution of excitation energy within the host lattice, contributing to improved excitation channel efficiency and enhanced overall luminescence performance. This interpretation is consistent with previous experimental studies and theoretical models describing $Ce^{3+} \leftrightarrow Tb^{3+}$ energy transfer mechanism.[35,36]

The onset of thermal quenching progressively shifts toward lower temperatures, decreasing from 660 K in YAG:Ce ceramics to 600 K in YAG:Ce,Tb10% ceramics. Notably, even with 10% Tb^{3+} ions, the ceramics retain good thermal stability. This luminescence quenching is primarily attributed to a thermally induced crossover from the excited-state $5d_1$ potential energy to the ground-state 4f potential energy, which facilitates nonradiative relaxation processes.[31,48]

Fig. 10b shows the temperature dependence of the decay times of Ce^{3+} emission at 530 nm under excitation into the $4f \rightarrow 5d_1$ transition of Ce^{3+} at 450 nm. For the undoped sample and the YAG:Ce,Tb1% sample, the effective decay time of Ce^{3+} emission remains relatively constant around 60 ns up to 480 K. Above this temperature, the decay rate accelerates significantly due to thermal quenching. As the temperature and Tb^{3+} ions concentration increase, the effective decay time of Ce^{3+} ions emission first increases, but after reaching approximately 380 K, a noticeable acceleration is observed. This temperature-dependent behavior varies between lightly and moderately Tb^{3+}-codoped samples and can be attributed to bidirectional energy transfer efficiency between coupled Tb^{3+} and Ce^{3+} ions, which becomes increasingly efficient with rising Tb^{3+} concentration. This effect likely influences the luminescence properties by facilitating nonradiative energy transfer processes within the material. As temperature increases, phonon interactions effectively bridge the energy gap between the Ce^{3+} ($5d_1$) and Tb^{3+} ($^5D_4$) states, bringing them into resonance and thereby facilitating a bidirectional energy transfer process. Consequently, higher temperatures promote the formation of Ce^{3+}–Tb^{3+} pairs, which leads to an extended effective decay time. Notably, this phonon-assisted resonance achieves optimal efficiency at temperatures above 480 K, further enhancing the overall energy transfer rate. The temperature dependence of photoluminescence effective decay times of Ce^{3+} ($5d_1 \rightarrow 4f$) emissions at 530 nm under excitation into $4f \rightarrow 5d_1$ absorption band of Tb^{3+} at 281 nm in YAG:Ce,Tbx% (x = 5 and 10) samples are shown in Fig. 10b. The observed differences in the effective decay time of Ce^{3+} emission at 530 nm under excitation at 450 nm (Ce^{3+} excitation) and 281 nm (Tb^{3+} excitation) result from variations in the rate and extent of energy migration between Tb^{3+} ions. In the first case, when Ce^{3+} ions are directly excited at 450 nm, the excitation energy is efficiently transferred between Ce^{3+} and Tb^{3+} ions, which are already in resonance. As a result, this energy transfer process is highly efficient and occurs rapidly. In contrast, when excitation occurs at 281 nm (Tb^{3+} excitation), the energy initially migrates among Tb^{3+} ions until it reaches a Tb^{3+} ion that is in resonance with a Ce^{3+} ion, allowing for the final energy transfer step. In other words, the Tb^{3+} sublattice actively seeks a suitable Tb^{3+} ion that is in resonance with Ce^{3+} ions, making the energy transfer process slower. Thus, this mechanism requires additional time due to the intermediate energy migration among Tb^{3+} ions before reaching a Ce^{3+} ion capable of accepting the excitation energy.

3.5. Scintillation properties

Fig. 11a presents the scintillation decay time recorded under γ-ray excitation (662 keV, ^{137}Cs radioisotope source). The decay times exhibit two exponential components: a fast component (τ_1) and a slow component (τ_2), both demonstrating strong dependence on Tb^{3+} ion concentration, see Table 3. In the Tb^{3+}-free YAG:Ce sample, the fast decay component (τ_1 = 44 ns) exhibits a slightly shorter decay time compared to the characteristic emission of isolated Ce^{3+} ions in garnet structures (typically 50–60 ns).[49] This observation aligns with the photoluminescence data, providing further evidence for Ce^{3+} emission quenching in Ce^{3+}–Ce^{3+} clusters and through interactions with structural defects (refer to Fig. 6 and associated discussion). The slow decay component (τ_2 = 155 ns) is attributed to the interaction of charge carriers (free holes and electrons) with intrinsic lattice defects, predominantly Y_{Al}^{x} antisite defects,[50] which significantly delay the scintillation response time. The YAG:Ce,Tb1% sample exhibits a fast scintillation decay component of τ_1 = 56 ns, while YAG:Ce,Tbx% (x = 5 and 10) samples demonstrate fast decay components of τ_1 = 67 ns. These decay time values are notably shorter compared to previously reported values of 78–80 ns in YAG:Ce 0.5% ceramics.[12,51,52] This improvement can be attributed to the more homogeneous spatial distribution of Ce^{3+} ions and reduced Ce^{3+}–Ce^{3+} clustering at grain boundaries. Additionally, the acceleration of decay kinetics may be facilitated by bidirectional Tb^{3+}-to-Ce^{3+} energy transfer process cycles. The dynamics of the slow scintillation decay component (τ_2) exhibit strong concentration dependence on Tb^{3+} content, as detailed in Table 4. This conclusion is further supported by pulse-height spectra analysis, see Fig. 11b and Table 4. The observed decrease in light yield (LY) with increasing Tb^{3+} concentration suggests that a portion of the excitation energy involved in the bidirectional Tb^{3+}-to-Ce^{3+} energy transfer cycles undergoes radiative recombination *via* Ce^{3+} centers beyond the 2 μs time gate used in LY measurements. Additionally, some of the charged carriers (electrons and holes) may undergo radiative recombination with Tb^{4+} ions beyond the 2 μs time gate used for LY measurements. This process suggests that the recombination dynamics contribute to the overall scintillation response and may play a role in influencing the observed LY characteristics of the material.

Fig. 12 shows the RL spectra of the YAG:Ce,Tbx% (x = 0, 1, 5 and 10) ceramics, exhibiting trends similar to those observed in the PL spectra (Fig. 5). In YAG crystals doped with 0.5% Ce^{3+}, a broad emission band centered at 530 nm is observed, corresponding to the Ce^{3+} $5d_1 \rightarrow 4f$ emission transition. Co-doping

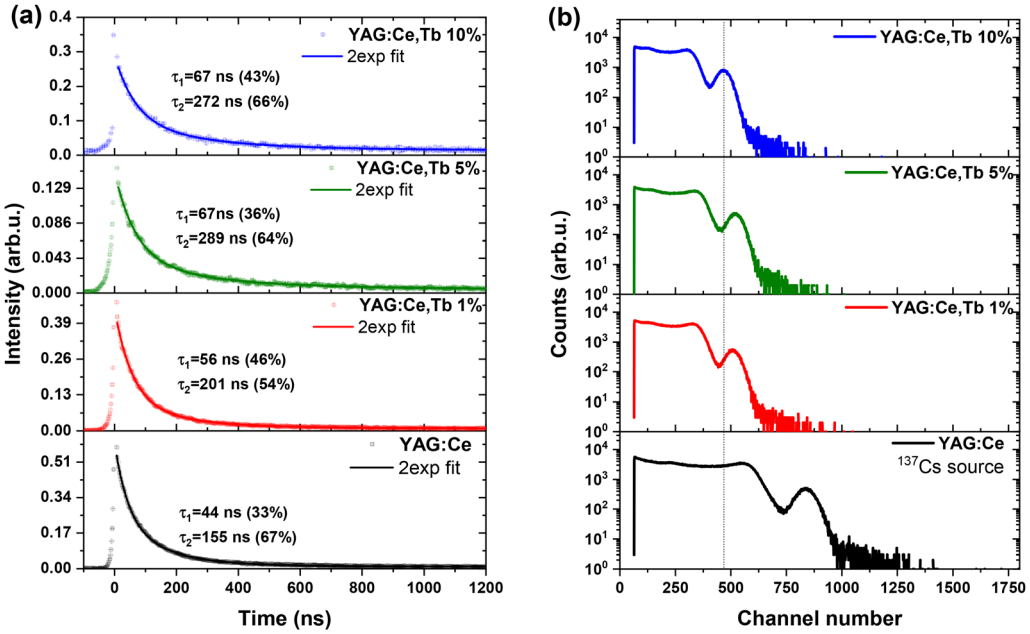

Fig. 11 (a) Scintillation decay times measured within 1 μs range and (b) pulse-height spectra measured with 2 μs shaping time under excitation with 662 keV γ-rays from a ^{137}Cs source for YAG:Ce,Tb*x*% (*x* = 0, 1, 5 and 10) ceramics.

Table 4 Scintillation parameters of YAG:Ce,Tb*x*% (*x* = 0, 1, 5 and 10) ceramics (2 μs shaping time). LY-light yield, *R*-energy resolution

Sample	LY (ph MeV^{-1})	%*R*	τ_1 ns (I%)	τ_2 ns (I%)	$\tau_{effective}$ (ns)
YAG:Ce	10 200	10.6%	44.6 (33%)	155.7 (67%)	119
YAG:Tb5%	6250	13.1%	56.2 (46%)	201.6 (54%)	135s
YAG:Ce,Tb1%	6370	12.4%	67.0 (36%)	289.3 (64%)	209
YAG:Ce,Tb5%	5700	13.8%	67.6 (43%)	272.6 (57%)	203

with Ce^{3+} and Tb^{3+} ions in YAG results in the spectral overlap of the Ce^{3+} emission and the characteristic Tb^{3+} 4f → 4f emission lines. The YAG:Ce,Tb1% sample exhibits a prominent emission line centered at 385 nm, corresponding to the characteristic $^5D_3$ → $^7F_5$ transition of Tb^{3+} ions. However, the emission intensity decreases notably with increasing Tb^{3+} concentration, primarily due to the cross-relaxation process occurring between Tb^{3+} pairs. This behavior is consistent with the trends observed in the PL. In contrast, the emission intensity from the $^5D_4$ energy state of Tb^{3+} ions increases significantly with rising Tb^{3+} concentration. This enhancement can be attributed to the more efficient energy migration and transfer processes between Tb^{3+} ions at higher doping levels, leading to stronger luminescence. Fig. 12b presents the integrated RL intensity (350–700 nm range) for the studied YAG:Ce,Tb*x*% ceramics. The integrated RL intensity gradually increases with the rising concentration of Tb^{3+} ions. The obtained result can be attributed to the increased density of emission centers within the garnet host lattice. As more Tb^{3+} ions are introduced into the garnet lattice, the number of emitting ions per unit volume rises, allowing for more efficient excitation and radiative decay processes. This results in a greater number of available radiative transitions, leading to a significant luminescence enhancement (Fig. 12b) Furthermore, the closer proximity of these ions facilitates energy transfer between them, contributing to the higher intensity of the emitted light.

3.6. Photoconversion properties

Based on the absorption spectra analysis, a 455 nm LED was used as the excitation source for photoconversion measurements. This wavelength corresponds to the maximum absorption band of Ce^{3+} ions. The measurements were conducted in a transmission setup, with ceramic samples of 1 mm thickness. The photoconversion spectra are presented in Fig. 13. A broadening of the LED emission line with a local maximum at 470 nm is observed, remaining consistent across all ceramic samples. The conversion of blue radiation into broadband emission, peaking at approximately 550 nm, is evident, as discussed in Section 3.2. Furthermore, the presence of Tb^{3+} ions influences the efficiency of blue radiation conversion into broadband emission. Specifically, with increasing Tb^{3+} concentration, the intensity of Ce^{3+} emission is enhanced, indicating an interaction between Tb^{3+} and Ce^{3+} that affects the luminescence properties of the ceramics. This effect translates into the correlated color temperature (CCT) of the emitted light, which reaches a maximum of 6013 K for YAG:Ce,Tb10% sample. The Tb^{3+}-free sample exhibits a CCT of 7639 K. As demonstrated on the CIE chromaticity diagram, doping with Tb^{3+} ions enables tuning of the light source's correlated color temperature. The color rendering index for all examined ceramics remains within a range of 69–73. Additionally, the luminous efficacy is similar for all samples, reaching approximately 120 lm W^{-1} (Table 5).

Fig. 13c shows a representative spectrum under 445 nm LD excitation for YAG:Ce. Due to the much narrower FWHM of the

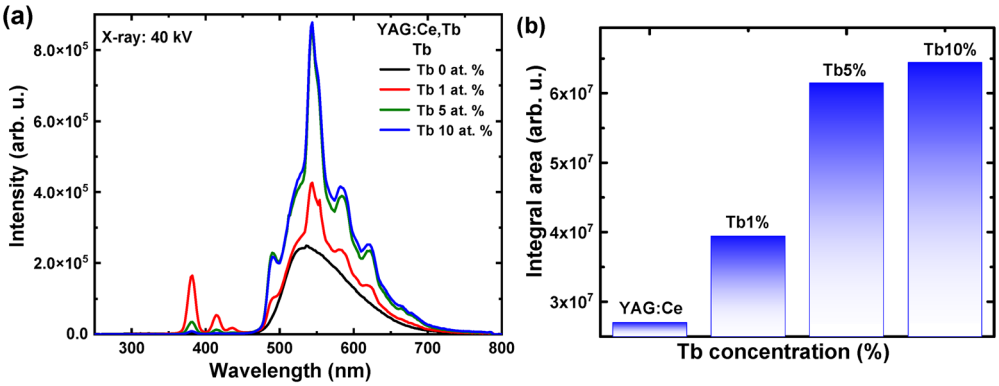

Fig. 12 (a) RL spectra for YAG:Ce,Tb*x*% (*x* = 0, 1, 5 and 10) ceramic samples; (b) integrated RL intensity in the spectral range 350–700 nm.

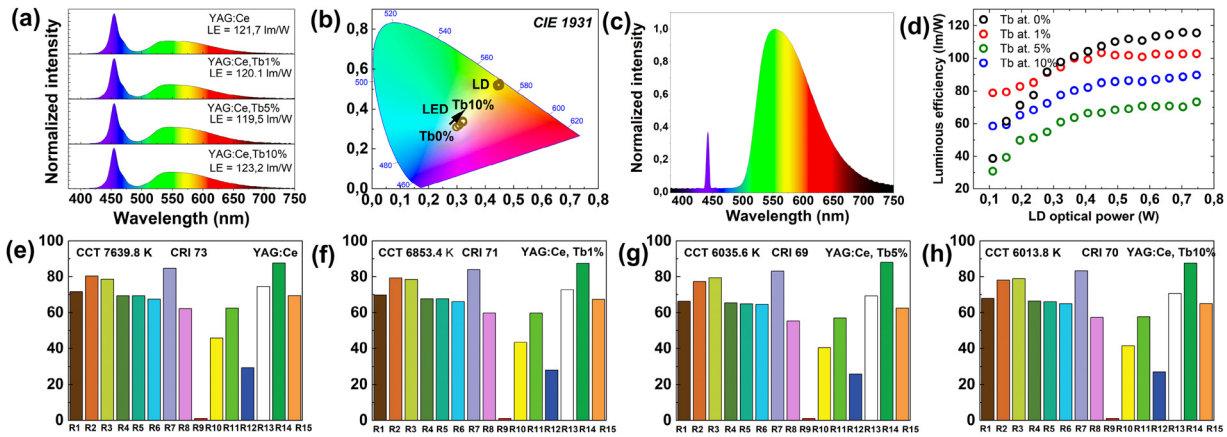

Fig. 13 Photoconversion properties of YAG:Ce,Tb*x*% (Tb = 0, 1, 5 and 10) ceramics: spectrum under LED excitation (a), CIE 1931 diagram of LED and LD excited samples (b) representative spectrum of YAG:Ce under LD excitation (c) influence of optical power on optical luminous efficiency (d) CRI of YAG:Ce,Tb*x*% (*x* = 0, 1, 5 and 10) ceramic samples (e–h).

Table 5 Photoconversion parameters of YAG:Ce,Tb*x*% (*x* = 0, 1, 5 and 10) ceramics under 455 nm LED excitation

	Photoconversion parameters			
Composition	CCT (K)	CRI	LE (lm W^{-1})	Year/Ref.
YAG:Ce ceramics	5528	62.8	122.4	2021/ref. 53
Al_2O_3/Al_2O_3–YAG:Ce/YAG composite	6615	69.9	126	2024/ref. 54
YAG:Ce	7639	73	121.7	This work
YAG:Ce,Tb1%	6853	71	120.1	This work
YAG:Ce,Tb5%	6035	69	119.5	This work
YAG:Ce,Tb10%	6013	70	123.2	This work

excitation source and consequently less coverage in the blue range – CRI values do not exceed 55 for any sample in the transmissive configuration, and the emission color is yellowish-white (Fig. 13b). The effect of excitation power on luminescence efficiency is shown in Fig. 13d. It is shown that the efficiency is not a constant parameter and depends on the excitation power. An increase in efficiency is observed up to a power of 0.5 W, followed by saturation. This effect agrees with the increase in sample temperature described in Section 3.4.

4. Conclusions

The YAG:Ce,Tb*x*% (0.5, 1, 10) transparent ceramics were successfully fabricated using the vacuum reactive sintering technique. The progressive increase in lattice constants from 12.608 Å in YAG:Ce ceramics to 12.615 Å in YAG:Ce,Tb10%, in accordance with Vegard's law, confirmed the effective incorporation of Tb^{3+} ions into dodecahedral crystallographic sites within the cubic garnet structure. SEM analysis revealed a fully densified microstructure without detectable micropores, either at triple grain boundaries or within grain interiors, which enabled high transparency. These ceramics exhibited an optical transmittance of 77–80% at 900 nm. Furthermore, their high transparency in the NIR-to-IR region positions them as promising candidates for applications as NIR-to-IR optical windows. Analysis of photoluminescence excitation and emission spectra revealed a strong dependence of the $Ce^{3+} \leftrightarrow Tb^{3+}$ bidirectional energy transfer efficiency on Tb^{3+} ions concentration. With increasing temperature, phonon interactions bridged the energy mismatch between Ce^{3+} and Tb^{3+} ions, enhancing the resonance condition and increasing the concentration of Tb^{3+}–Ce^{3+} pairs. This resonance led to improved energy transfer

efficiency from Tb^{3+} to Ce^{3+} ions. The incorporation of Tb^{3+} ions resulted in a modest reduction in the thermal stability of Ce^{3+} emission, however, the overall stability remained at a high level. The bidirectional energy transfer significantly prolonged the effective decay time, reaching an optimal value at approximately 480 K. Above this temperature, the transfer rate accelerated further, demonstrating the temperature-driven enhancement of the energy conversion process. Scintillation decay times measured within the 1 μs range confirmed the acceleration of both fast and slow decay components due to the Tb^{3+}–Ce^{3+} energy transfer. However, the light yield measurements indicated a decline with increasing Tb^{3+} concentration, attributed to radiative recombination *via* Ce^{3+} centers as well as Tb^{3+} and Tb^{3+} ions occurring beyond the 2 μs time gate. Despite this, compared to undoped samples, the YAG:Ce,Tb10% ceramics demonstrated a remarkable two-fold increase in radioluminescence intensity measured within 1 s time gate, attributed to the higher density of emitting centers and collected light from all Tb^{3+} ions with recombination time of hundreds ms. This enhancement underscores the potential of YAG:Ce,Tb transparent ceramics in X-ray imaging applications. The codoping of YAG:Ce ceramics with Tb^{3+} ions also proved effective in enhancing photoconversion properties. Increasing Tb^{3+} concentration elevated Ce^{3+} emission and enabled tuning of the correlated color temperature (CCT). While the optimal CCT of 6013 K was observed for YAG:Ce,Tb10%, the Tb^{3+}-free sample exhibited a higher CCT of 7639 K. The color rendering index (CRI) remained stable in the range of 69–73 across all samples, and luminous efficacy was consistently maintained at approximately 120 lm W^{-1}, regardless of composition. Under 455 nm laser excitation, luminescence efficiency rises with power up to 0.5 W and then saturates. The narrow FWHM of the laser limits blue light coverage, resulting in CRI values below 55 for all samples and a yellowish-white emission color. These results highlight the potential of YAG:Ce,Tb transparent ceramics as materials for X-ray imaging and white phosphors for LED applications.

Conflicts of interest

The authors declare no conflict of interest.

Data availability

All raw data supporting the findings of this study are available in the ASEP repository (Institute of Physics of the Czech Academy of Sciences, Prague, Czech Republic) at **https://doi.org/10.57680/asep.0639828**.

Supplementary information (SI) is available. See DOI: **https://doi.org/10.1039/d5ma00464k**.

Acknowledgements

This work was supported by the National Science Centre Poland (NCN) MINIATURA Grant No. 2024/08/X/ST5/00814. Support from the European Union's Horizon Europe research and innovation program under the Marie Skłodowska-Curie Actions COFUND, Physics for Future, grant agreement No 101081515 and the Postdoctoral fellowship project of the Research Council of Lithuania (No. S-PD-24-63) is also gratefully acknowledged.

References

1 C. Ronda, Scintillators for medical imaging, *Opt. Mater. X*, 2024, **22**, 100293, DOI: **10.1016/j.omx.2024.100293**.
2 S. J. Duclos, Scintillator Phosphors for Medical Imaging, Electrochem, *Soc. Interface*, 1998, **7**, 34–38, DOI: **10.1149/2.F07982IF**.
3 C. Michail, P. Liaparinos, N. Kalyvas, I. Kandarakis, G. Fountos and I. Valais, Phosphors and Scintillators in Biomedical Imaging, *Crystals*, 2024, **14**, 169, DOI: **10.3390/cryst14020169**.
4 P. Lecoq, Development of new scintillators for medical applications, *Nucl. Instrum. Methods Phys. Res., Sect. A*, 2016, **809**, 130–139, DOI: **10.1016/j.nima.2015.08.041**.
5 Z. Wang, C. Dujardin, M. S. Freeman, A. E. Gehring, J. F. Hunter, P. Lecoq, W. Liu, C. L. Melcher, C. L. Morris, M. Nikl, G. Pilania, R. Pokharel, D. G. Robertson, D. J. Rutstrom, S. K. Sjue, A. S. Tremsin, S. A. Watson, B. W. Wiggins, N. M. Winch and M. Zhuravleva, Needs, Trends, and Advances in Scintillators for Radiographic Imaging and Tomography, *IEEE Trans. Nucl. Sci.*, 2023, **70**, 1244–1280, DOI: **10.1109/TNS.2023.3290826**.
6 D. Chu, B. Jia, N. Liu, Y. Zhang, X. Li, J. Feng, J. Pi, Z. Yang, G. Zhao, Y. Liu, S. (Frank) Liu and N.-G. Park, Lattice engineering for stabilized black $FAPbI_3$ perovskite single crystals for high-resolution x-ray imaging at the lowest dose, *Sci. Adv.*, 2023, **9**, eadh2255, DOI: **10.1126/sciadv.adh2255**.
7 W. Ma, T. Jiang, Z. Yang, H. Zhang, Y. Su, Z. Chen, X. Chen, Y. Ma, W. Zhu, X. Yu, H. Zhu, J. Qiu, X. Liu, X. Xu and Y. (Michael) Yang, Highly Resolved and Robust Dynamic X-Ray Imaging Using Perovskite Glass-Ceramic Scintillator with Reduced Light Scattering, *Adv. Sci.*, 2021, **8**, 2003728, DOI: **10.1002/advs.202003728**.
8 J. Liu, X. Zhao, Y. Xu, H. Wu, X. Xu, P. Lu, X. Zhang, X. Zhao, M. Xia, J. Tang and G. Niu, All-Inorganic Glass Scintillators: Scintillation Mechanism, Materials, and Applications, *Laser Photonics Rev.*, 2023, **17**, 2300006, DOI: **10.1002/lpor.202300006**.
9 T. Ji, T. Wang, H. Li, Q. Peng, H. Tang, S. Hu, A. Yakovlev, Y. Zhong and X. Xu, Ce^{3+} -Doped Yttrium Aluminum Garnet Transparent Ceramics for High-Resolution X-Ray Imaging, *Adv. Opt. Mater.*, 2022, **10**, 2102056, DOI: **10.1002/adom.202102056**.
10 P. Ctibor, J. Sedláček and T. Hudec, Dielectric properties of Ce-doped YAG coatings produced by two techniques of plasma spraying, *Bol. Soc. Esp. Cerámica Vidr.*, 2022, **61**, 408–416, DOI: **10.1016/j.bsecv.2021.02.002**.
11 *Recent advances in ceramic materials research*, ed. J. J. R. Rovira, Nova Science Publ, New York, 2013.

12 T. Yanagida, H. Takahashi, T. Ito, D. Kasama, T. Enoto, M. Sato, S. Hirakuri, M. Kokubun, K. Makishima, T. Yanagitani, H. Yagi, T. Shigeta and T. Ito, Evaluation of properties of YAG (Ce) ceramic scintillators, *IEEE Trans. Nucl. Sci.*, 2005, **52**, 1836–1841, DOI: **10.1109/TNS.2005.856757**.

13 X. Liu, X. Wang and Z. Wang, Selectively excited emission and Tb 3 + → Ce 3 + energy transfer in yttrium aluminum garnet, *Phys. Rev. B: Condens. Matter Mater. Phys.*, 1989, **39**, 10633–10639, DOI: **10.1103/PhysRevB.39.10633**.

14 K. Bartosiewicz, V. Babin, J. A. Mares, A. Beitlerova, Y. Zorenko, A. Iskaliyeva, V. Gorbenko, Z. Bryknar and M. Nikl, Luminescence and energy transfer processes in Ce 3+ activated (Gd,Tb) 3 Al 5 O 12 single crystalline films, *J. Lumin.*, 2017, **188**, 60–66, DOI: **10.1016/j.jlumin.2017.04.010**.

15 J. M. Ogiegło, A. Zych, K. V. Ivanovskikh, T. Jüstel, C. R. Ronda and A. Meijerink, Luminescence and Energy Transfer in Lu $_3$ Al $_5$ O $_{12}$ Scintillators Co-Doped with Ce^{3+} and Tb^{3+}, *J. Phys. Chem. A*, 2012, **116**, 8464–8474, DOI: **10.1021/jp301337f**.

16 Y. Ma, L. Zhang, T. Zhou, B. Sun, Q. Yao, P. Gao, J. Huang, J. Kang, F. A. Selim, C. Wong, H. Chen and Y. Wang, Weak thermal quenching and tunable luminescence in Ce:Y3-(Al,Sc)5O12 transparent ceramics for high power white LEDs/LDs, *Chem. Eng. J.*, 2020, **398**, 125486, DOI: **10.1016/j.cej.2020.125486**.

17 S. Li, Y. Guo and R.-J. Xie, Laser Phosphors for Next-Generation Lighting Applications, *Acc. Mater. Res.*, 2022, **3**, 1299–1308, DOI: **10.1021/accountsmr.2c00193**.

18 L. Wang, Y. Li, X. Li, Y. Zhu, C. Zhang, J. Kang, C. Shao, L. Zhang and J. Zou, Laser light illuminant based on YAG: Ce phosphor ceramic with ultra-high luminance, stable output, and excellent heat dissipation, *Opt. Mater.*, 2024, **157**, 116410, DOI: **10.1016/j.optmat.2024.116410**.

19 Q.-Q. Zhu, S. Li, Q. Yuan, H. Zhang and L. Wang, Transparent YAG:Ce ceramic with designed low light scattering for high-power blue LED and LD applications, *J. Eur. Ceram. Soc.*, 2021, **41**, 735–740, DOI: **10.1016/j.jeurceramsoc.2020.09.006**.

20 J. Chen, Y. Tang, X. Yi, Y. Tian, G. Ao, D. Hao, Y. Lin and S. Zhou, Fabrication of $(Tb,Gd)_3$ Al_5 O_{12}:Ce^{3+} phosphor ceramics for warm white light-emitting diodes application, *Opt. Mater. Express*, 2019, **9**, 3333, DOI: **10.1364/OME.9.003333**.

21 A. Markovskyi, V. Gorbenko, T. Zorenko, K. Bartosiewicz, A. Fedorov and Y. Zorenko, Development of $Tb_{1.5}Gd_{1.5}Al_5O_{12}$:Ce Single-Crystalline Film Converters for WLED Using a Liquid Phase Epitaxy Growth Method, *Crystals*, 2022, **12**, 1814, DOI: **10.3390/cryst12121814**.

22 M. Gong, W. Xiang, X. Liang, J. Zhong, D. Chen, J. Huang, G. Gu, C. Yang and R. Xiang, Growth and characterization of air annealing Tb-doped YAG:Ce single crystal for white-light-emitting diode, *J. Alloys Compd.*, 2015, **639**, 611–616, DOI: **10.1016/j.jallcom.2015.03.162**.

23 R. D. Shannon, Revised effective ionic radii and systematic studies of interatomic distances in halides and chalcogenides, *Acta Crystallogr. Sect. A*, 1976, **32**, 751–767, DOI: **10.1107/S0567739476001551**.

24 B. Strocka, P. Holst and W. Tolksdorf, Empirical formula for the calculation of lattice constants of oxide garnets based on substituted yttrium- and gadolinium-iron garnets, *Philips Res. Rep.*, 1978, **33**, 186–202.

25 S. Geller, G. P. Espinosa, L. D. Fullmer and P. B. Crandall, Thermal expansion of some garnets, *Mater. Res. Bull.*, 1972, **7**, 1219–1224, DOI: **10.1016/0025-5408(72)90101-8**.

26 S. Geller, Crystal chemistry of the garnets, Z. Für Krist.-Cryst, *Mater.*, 1967, **125**, 1–47.

27 M. O. Ramirez, J. Wisdom, H. Li, Y. L. Aung, J. Stitt, G. L. Messing, V. Dierolf, Z. Liu, A. Ikesue, R. L. Byer and V. Gopalan, Three-dimensional grain boundary spectroscopy in transparent high power ceramic laser materials, *Opt. Express*, 2008, **16**, 5965–5973, DOI: **10.1364/OE.16.005965**.

28 A. D. Timoshenko, O. O. Matvienko, A. G. Doroshenko, S. V. Parkhomenko, I. O. Vorona, O. S. Kryzhanovska, N. A. Safronova, O. O. Vovk, V. Tolmachev, V. N. Baumer, I. Matolínová, S. Hau, C. Gheorghe and R. P. Yavetskiy, Highly-doped YAG:Sm3+ transparent ceramics: Effect of Sm3+ ions concentration, *Ceram. Int.*, 2023, **49**, 7524–7533, DOI: **10.1016/j.ceramint.2022.10.257**.

29 X. Li, J. Yin, S. Yu, X. Zhang and Y. Lai, Microstructure of Nd:YAG transparent dielectric ceramics with ultra-high-quality factor, *J. Adv. Dielectr.*, 2024, **14**, 2440001, DOI: **10.1142/S2010135X24400010**.

30 W. Wongwan, P. Yasaka, K. Boonin, W. Sa-ardsin and J. Kaewkhao, Structural and Luminescence Characterizations of Tb^{3+} Ion Doped Boro-Tellurite Glasses for LED Applications, *Integr. Ferroelectr.*, 2022, **224**, 62–70, DOI: **10.1080/10584587.2022.2035596**.

31 K. Bartosiewicz, A. Szysiak, R. Tomala, P. Gołębiewski, H. Węglarz, V. Nagirnyi, M. Kirm, I. Romet, M. Buryi, V. Jary, R. Kucerkova, M. Wzorek and R. Buczyński, Energy-Transfer Processes in Nonstoichiometric and Stoichiometric Er^{3+}, Ho^{3+}, Nd^{3+}, Pr^{3+}, and Cr^{3+}-Codoped Ce:YAG Transparent Ceramics: Toward High-Power and Warm-White Laser Diodes and LEDs, *Phys. Rev. Appl.*, 2023, **20**, 014047, DOI: **10.1103/PhysRevApplied.20.014047**.

32 T. Wu, L. Wang, Y. Shi, X. Huang, Q. Zhang, Y. Xiong, H. Wang, J. Fang, J. Ni, H. He, C. Wang, Z. Zhou, Q. Liu, Q. Li, J. Yu, O. Shichalin and E. Papynov, Wide Concentration Range of Tb3+ Doping Influence on Scintillation Properties of $(Ce, Tb, Gd)_3Ga_2Al_3O_{12}$ Crystals Grown by the Optical Floating Zone Method, *Materials*, 2022, **15**, 2044, DOI: **10.3390/ma15062044**.

33 V. Babin, V. Gorbenko, A. Makhov, J. A. Mares, M. Nikl and S. Zazubovich, Yu. Zorenko, Luminescence characteristics of Pb^{2+} centres in undoped and Ce^{3+} -doped $Lu_3Al_5O_{12}$ single-crystalline films and Pb^{2+} → Ce^{3+} energy transfer processes, *J. Lumin.*, 2007, **127**, 384–390, DOI: **10.1016/j.jlumin.2007.01.011**.

34 A. Markovskyi, W. Gieszczyk, P. Bilski, A. Fedorov, K. Bartosiewicz, K. Paprocki, T. Zorenko and Y. Zorenko, Composition engineering of $Tb_{3-x}Gd_xAl_{5-y}GayO_{12}$:Ce single

crystals and their luminescent, scintillation and photoconversion properties, *J. Alloys Compd.*, 2020, **849**, 155808, DOI: 10.1016/j.jallcom.2020.155808.

35 K. Omuro, M. Yoshino, K. Bartosiewicz, T. Horiai, R. Murakami, K. J. Kim, K. Kamada, R. Kucerkova, V. Babin, M. Nikl, A. Yamaji, T. Hanada, Y. Yokota, S. Kurosawa, Y. Ohashi, H. Sato and A. Yoshikawa, Insights into luminescence and energy transfer processes in Ce^{3+} - and Tb^{3+} co-doped $(Gd, Y)_3Al_2Ga_3O_{12}$ garnet single crystals, *J. Lumin.*, 2024, **273**, 120663, DOI: 10.1016/j.jlumin.2024.120663.

36 K. Bartosiewicz, R. Tomala, D. Szymański, B. Albini, J. Zeler, M. Yoshino, T. Horiai, P. Socha, S. Kurosawa, K. Kamada, P. Galinetto, E. Zych and A. Yoshikawa, Micro-Inclusion Engineering via Sc Incompatibility for Luminescence and Photoconversion Control in Ce^{3+} -Doped $Tb_3Al_{5-x}Sc_xO_{12}$ Garnet, *Materials*, 2024, **17**, 2762, DOI: 10.3390/ma17112762.

37 D. J. Robbins, B. Cockayne, B. Lent and J. L. Glasper, The mechanism of cross-relaxation in $Y_3Al_5O_{12}:Tb^{3+}$, *Solid State Commun.*, 1976, **20**, 673–676, DOI: 10.1016/0038-1098(76)90743-2.

38 J. Liu, Q. Song, D. Li, Y. Ding, X. Xu and J. Xu, Spectroscopic properties of $Tb:Y_3Al_5O_{12}$ crystal for visible laser application, *Opt. Mater.*, 2020, **106**, 110001, DOI: 10.1016/j.optmat.2020.110001.

39 V. Laguta, M. Buryi, S. Tkachenko, P. Arhipov, I. Gerasymov, O. Sidletskiy, O. Laguta and M. Nikl, Oxygen-vacancy centers in $Y_3Al_5O_{12}$ garnet crystals: electron paramagnetic resonance and dielectric spectroscopy study, *Phys. Rev. B*, 2020, **101**, 024106, DOI: 10.1103/PhysRevB.101.024106.

40 L. Jia, J. Zhu, Y. Boyaryntseva, I. Gerasymov, B. Grynyov and O. Sidletskiy, Effect of Carbon Doping on F-Type Defects in YAG and YAG:Ce Crystals, *Phys. Status Solidi B*, 2021, **258**, 2100325, DOI: 10.1002/pssb.202100325.

41 Y. Dong, J. Xu, G. Zhou, G. Zhao, L. Su, X. Xu, H. Li, J. Si, X. Qian, X. Li and J. Shen, Color centers in Yb:YAG crystals grown by temperature-gradient techniques, *Phys. Status Solidi A*, 2006, **203**, 2496–2500, DOI: 10.1002/pssa.200521223.

42 S. P. Feofilov, A. B. Kulinkin, T. Gacoin, G. Mialon, G. Dantelle, R. S. Meltzer and C. Dujardin, Mechanisms for Ce^{3+} excitation at energies below the zero-phonon line in YAG crystals and nanocrystals, *J. Lumin.*, 2012, **132**, 3082–3088, DOI: 10.1016/j.jlumin.2012.06.030.

43 S. Agarwal, M. S. Haseman, A. Khamehchi, P. Saadatkia, D. J. Winarski and F. A. Selim, Physical and optical properties of Ce:YAG nanophosphors and transparent ceramics and observation of novel luminescence phenomenon, *Opt. Mater. Express*, 2017, **7**, 1055, DOI: 10.1364/OME.7.001055.

44 S. P. Feofilov, A. B. Kulinkin, T. Gacoin, G. Mialon, G. Dantelle, R. S. Meltzer and C. Dujardin, Mechanisms for Ce^{3+} excitation at energies below the zero-phonon line in YAG crystals and nanocrystals, *J. Lumin.*, 2012, **132**, 3082–3088, DOI: 10.1016/j.jlumin.2012.06.030.

45 K. V. Ivanovskikh, J. M. Ogiegło, A. Zych, C. R. Ronda and A. Meijerink, Luminescence Temperature Quenching for Ce^{3+} and Pr^{3+} d-f Emission in YAG and LuAG, *ECS J. Solid State Sci. Technol.*, 2013, **2**, R3148–R3152, DOI: 10.1149/2.011302jss.

46 Y.-C. Lin, M. Bettinelli and M. Karlsson, Unraveling the Mechanisms of Thermal Quenching of Luminescence in Ce^{3+} -Doped Garnet Phosphors, *Chem. Mater.*, 2019, **31**, 3851–3862, DOI: 10.1021/acs.chemmater.8b05300.

47 K. Asami, J. Ueda, M. Shiraiwa, K. Fujii, M. Yashima and S. Tanabe, Redshift and thermal quenching of Ce3+ emission in (Gd, Y)3(Al, Si)5(O, N)12 oxynitride garnet phosphors, *Opt. Mater.*, 2019, **87**, 117–121, DOI: 10.1016/j.optmat.2018.04.049.

48 V. Bachmann, C. Ronda and A. Meijerink, Temperature Quenching of Yellow Ce^{3+} Luminescence in YAG:Ce, *Chem. Mater.*, 2009, **21**, 2077–2084, DOI: 10.1021/cm8030768.

49 K. Bartosiewicz, A. Markovskyi, T. Horiai, D. Szymański, S. Kurosawa, A. Yamaji, A. Yoshikawa and Y. Zorenko, A study of Mg^{2+} ions effect on atoms segregation, defects formation, luminescence and scintillation properties in Ce^{3+} doped $Gd_3Al_2Ga_3O_{12}$ single crystals, *J. Alloys Compd.*, 2022, **905**, 164154, DOI: 10.1016/j.jallcom.2022.164154.

50 E. Mihóková, V. Babin, K. Bartosiewicz, L. S. Schulman, V. Čuba, M. Kučera and M. Nikl, Low temperature delayed recombination decay in scintillating garnets, *Opt. Mater.*, 2015, **40**, 127–131, DOI: 10.1016/j.optmat.2014.12.011.

51 E. Mihóková, M. Nikl, J. A. Mareš, A. Beitlerová, A. Vedda, K. Nejezchleb, K. Blažek and C. D'Ambrosio, Luminescence and scintillation properties of YAG:Ce single crystal and optical ceramics, *J. Lumin.*, 2007, **126**, 77–80, DOI: 10.1016/j.jlumin.2006.05.004.

52 H. Takahashi, T. Yanagida, D. Kasama, T. Ito, M. Kokubun, K. Makishima, T. Yanagitani, H. Yagi, T. Shigeta and T. Ito, The Temperature Dependence of Gamma-Ray Responses of YAG:Ce Ceramic Scintillators, *IEEE Trans. Nucl. Sci.*, 2006, **53**, 2404–2408, DOI: 10.1109/TNS.2006.878575.

53 A. Du, Q. Du, X. Liu, Y. Yang, C. Xia, J. Zou and J. Li, Ce:YAG Transparent Ceramics Enabling High Luminous Efficacy for High-power LEDs/LDs, *J. Inorg. Mater.*, 2021, **36**, 883, DOI: 10.15541/jim20200727.

54 P. Sang, L. Zhang, J. Kang, M. Li, S. Chen, P. Yang, B. Sun, Y. Li, W. Strek and H. Chen, Composite structure Al_2O_3/Al_2O_3–YAG:Ce/YAG ceramics with high color spatial uniformity for white laser lighting, *J. Adv. Ceram.*, 2024, **13**, 189, DOI: 10.26599/JAC.2024.9220840.